Observations of interstellar helium pickup ions in the inner heliosphere

Daniel J. Gershman,[1] George Gloeckler,[1] Jason A. Gilbert,[1] Jim M. Raines,[1] Lennard A. Fisk,[1] Sean C. Solomon,[2,3] Edward C. Stone,[4] and Thomas H. Zurbuchen[1]

Received 4 May 2012; revised 6 March 2013; accepted 10 March 2013; published 26 April 2013.

[1] During the MESSENGER spacecraft's interplanetary trajectory to Mercury, the Fast Imaging Plasma Spectrometer (FIPS) measured the first helium pickup ion distributions at a heliocentric distance (R) ranging between 0.3 and 0.7 AU. From several transits of MESSENGER through the interstellar helium gravitational focusing cone, we map the cone structure in the ecliptic at R = 0.3 AU and compare it with observations of He^+ at R = 1 AU made with the Solar Wind Ion Composition Spectrometer (SWICS) on the Advanced Composition Explorer (ACE). Average downwind enhancements of $\approx$ 8 and average cone widths of $\approx$ 30° measured by each sensor match known models of neutral helium during this most recent, unusually quiet, solar minimum. The average cone center direction is calculated to be at J2000 ecliptic longitude λ_∞ = 76.0°(±6.0°) and 77.0°(±1.5°) from FIPS and SWICS observations, respectively. These parameters are also in agreement with previous determinations of the downwind direction of interstellar flow and demonstrate the effectiveness of using pickup ion observations inside 1 AU to map the structure of the neutral helium distribution in the heliosphere, as well as to diagnose the conditions of the interstellar medium.

Citation: Gershman, D. J., G. Gloeckler, J. A. Gilbert, J. M. Raines, L. A. Fisk, S. C. Solomon, E. C. Stone, and T. H. Zurbuchen, (2013), Observations of interstellar helium pickup ions in the inner heliosphere, *J. Geophys. Res. Space Physics*, *118*, 1389–1402, doi:10.1002/jgra.50227.

1. Introduction

[2] As the Sun travels through the local interstellar medium (LISM), neutral gas flows into the heliosphere. These gas particles, consisting primarily of hydrogen and helium, follow ballistic trajectories through the solar system, guided only by the combined gravitational and radiation pressure forces of the Sun [*Fahr*, 1968; *Blum and Fahr*, 1970]. Near the Sun's vicinity, this neutral population is lost via ionization reactions, whereby neutral particles of the interstellar gas become ions that are embedded in and picked up by the constantly expanding solar atmosphere, the solar wind. Initial analytical studies of this process [*Blum and Fahr*, 1970; *Fahr*, 1971] focused on trajectories of interstellar neutral hydrogen. Because of substantial Lyman-α radiation pressure, a cavity devoid of interstellar hydrogen forms around the Sun [*Thomas*, 1978; *Fahr*, 1978]. For interstellar helium, however, which is largely unaffected by radiation pressure, the Sun acts as a gravitational lens, forming a neutral He focusing cone downwind from the direction of interstellar flow, as illustrated in Figure 1. This cone was first observed remotely through backscattered He 58.4 nm observations by an instrument on the Solrad 11 satellite [*Weller and Meier*, 1981]. The structure (i.e., width and peak density) of the cone is controlled only by the kinetic properties of the LISM neutral helium gas and the ionization rates of helium in the heliosphere [*Feldman et al.*, 1972; *Blum et al.*, 1975; *Meier*, 1977; *Thomas*, 1978; *Wu and Judge*, 1979].

[3] Ionized helium particles, although lost to the neutral population, are measured by spaceborne ion mass spectrometers as pickup ions. As first measured by *Möbius et al.* [1985], such observations are important not only for verifying the accuracy of the deduced properties and flow direction of the interstellar medium [*Möbius et al.*, 1995; *Möbius et al.*, 1996; *Noda et al.*, 2001; *Gloeckler and Geiss*, 2001; *Gloeckler et al.*, 2004], but also as a useful diagnostic for understanding the evolution of pickup ion distribution functions [*Gloeckler et al.*, 1995; *Gloeckler and Geiss*, 1998; *Saul et al.*, 2007], a physical process common in planetary magnetospheres [e.g., *Hartle et al.*, 1982; *Zurbuchen et al.*, 2008] or around comets [*Ipavich et al.*, 1986; *Neugebauer et al.*, 1989; *Gloeckler et al.*, 2000].

[4] The properties of the LISM helium have been constrained from in situ neutral [*Witte et al.*, 2004; *Möbius*

[1]Department of Atmospheric, Oceanic and Space Sciences, University of Michigan, Ann Arbor, Michigan, USA.
[2]Department of Terrestrial Magnetism, Carnegie Institution of Washington, Washington, D.C., USA.
[3]Lamont-Doherty Earth Observatory, Columbia University, Palisades, New York, USA.
[4]California Institute of Technology, Pasadena, California, USA.

Corresponding author: D. J. Gershman, Department of Atmospheric, Oceanic and Space Sciences, University of Michigan, Ann Arbor, MI, 48105, USA. (djgersh@umich.edu)

2169-9380/13/10.1002/jgra.50227

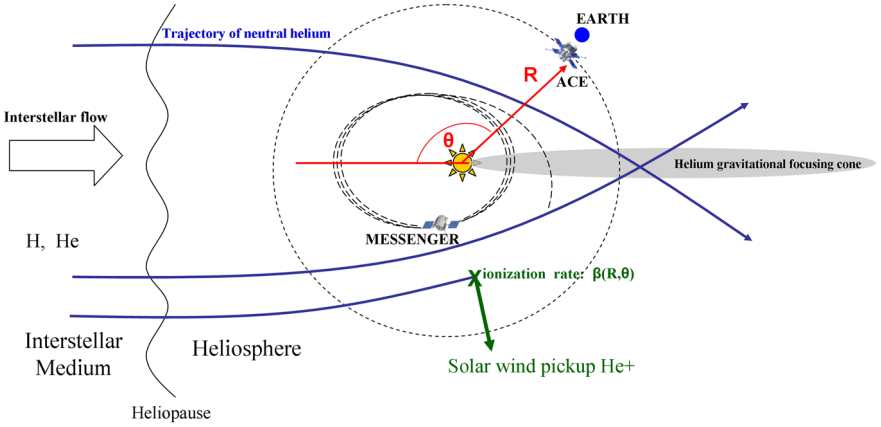

Figure 1. Illustration of the trajectories of neutral particles that converge to form the helium gravitational focusing cone directly downwind from the direction of interstellar flow. Neutral helium throughout the heliosphere can be ionized and injected into the solar wind as pickup ions that can be measured in situ by SWICS on ACE, which orbits the Sun at L1 (1 AU) and FIPS on MESSENGER, which passes through the focusing cone several times during its inner heliospheric passage to Mercury. The coordinates (R,θ) are defined as the heliocentric distance and the angle from the upwind direction of interstellar flow, respectively.

et al., 2012] and pickup ion [*Gloeckler et al.*, 2004] measurements and from remote sensing observations of helium glow [*Vallerga et al.*, 2004; *Lallement et al.*, 2004] and solar wind charge-exchange emission [*Koutroumpa et al.*, 2009] by the use of instrument forward models to fit observations. *Möbius et al.* [2004] summarized an effort to combine these results from different diagnostics to form a set of consistent parameters for the interstellar gas flow velocity vector and temperature in J2000 ecliptic coordinates, with a flow direction given by longitude λ_∞ = 75.38°(±0.56°) and latitude β_∞ = –5.31°(±0.28°), an inflow velocity v_∞ = 26.24(±0.45) km/s, and a temperature T_∞ = 6306(±390) K. However, new observations of energetic neutral particles from the Interstellar Boundary Explorer (IBEX) [*McComas et al.*, 2004a], have produced an alternate set of parameters of λ_∞ = 79.0°(+3.0°, –3.5°), β_∞ = –4.9°(±0.2°), velocity v_∞ = 23.5(+3.0°, –2.0°) km/s, [*Möbius et al.*, 2012] and $T_\infty \approx$ 6200 K [*Bzowski et al.*, 2012].

[5] To date, the only available He^+ pickup ion measurements have been at heliocentric distance $R \geq 1$ AU. In situ studies of the focusing cone have been limited to ecliptic measurements at 1 AU [*Möbius et al.*, 1995; *Möbius et al.*, 1996; *Noda et al.*, 2001; *Gloeckler and Geiss*, 2001; *Gloeckler et al.*, 2004; *Drews et al.*, 2010] and a single near-downwind pass near Jupiter [*McComas et al.*, 2004b] with the Cassini Plasma Spectrometer (CAPS) on the Cassini spacecraft [*Young et al.*, 2004].

[6] The Fast Imaging Plasma Spectrometer (FIPS), one of two charged particle sensors on the Energetic Particle and Plasma Spectrometer (EPPS) instrument [*Andrews et al.*, 2007] on the MErcury Surface, Space ENvironment, GEochemistry, and Ranging (MESSENGER) spacecraft [*Solomon et al.*, 2001] has yielded the first in situ measurements of He^+ inside of 1 AU and the first observations that span the full longitudinal structure of the gravitational focusing cone at heliocentric distances less than ~0.6 AU. Although also confined to the ecliptic plane, the spacecraft's cruise trajectory, as shown in Figure 1, led to several transits of the gravitational focusing cone inside 1 AU. This paper reports on our analysis of the unprecedented data set provided by FIPS during those observing opportunities. When combined with data from the Solar Wind Ion Composition Spectrometer (SWICS) instrument [*Gloeckler et al.*, 1998] on the Advanced Composition Explorer (ACE) spacecraft [*Stone et al.*, 1998], constraints on the transport and large-scale diffusion of He^+ ions within 1 AU can be developed to test the effectiveness of using near-Earth measurements to describe the longitudinal structure of neutral helium population in the heliosphere.

[7] It can be difficult to use pickup ion measurements to tightly constrain the direction of interstellar flow. Possible diffusive ion transport from the initial pickup location [*Möbius et al.*, 1995] and the influence of the ambient solar wind conditions on measured pickup ion densities [*Saul et al.*, 2003; *Möbius et al.*, 2010] can bias the determination of the cone center location for any given downwind pass. We argue here that some of this variability can be removed by averaging over multiple passes during times when the pickup ion production rate is expected to be steady state, i.e., near solar minimum.

[8] In section 2 of this paper, we discuss the interpretation of 1 AU pickup ion measurements. In section 3, we describe the most recent, unusually low solar minimum and why it is uniquely suited for using pickup ion measurements to map the neutral density distribution in the heliosphere. In section 4, we combine data from MESSENGER/FIPS and ACE/SWICS to analyze the gravitational focusing cone structure at R = 0.3 and 1 AU between 2007 and 2009. Finally, in section 5, we discuss the implications of these measurements for possible large-scale transport effects of pickup helium in the inner heliosphere.

2. Limitations of Pickup Ion Observations

[9] The abundance and dynamic state of pickup ion spectra at any heliocentric distance depend on (1) the neutral

density distribution throughout the heliosphere, (2) the ionization rate profile(s) for the production of new pickup ions, and (3) the evolution of pickup ion velocity distributions in space. Models of each of these processes have been developed and successfully used to match measurements at 1 AU, constraining important parameters of the underlying physical processes.

2.1. Neutral Density Distribution in the Heliosphere

[10] A complete heliospheric neutral helium model requires knowledge not only of the direction and properties of interstellar flow, but also of the radial, latitudinal, longitudinal, and time-dependent properties of ionization rates. Far (>1 AU) from the Sun, photoionization by extreme ultraviolet (EUV) photons is the dominant loss mechanism for helium. Losses associated with resonant charge-exchange reactions between neutral helium and solar wind protons and alpha particles are lower by an order of magnitude [*McMullin et al.*, 2004] and are neglected here. As a simplification, photoionization is sometimes modeled as spherically symmetric. However, there can be strong spatial variations in EUV coronal emissions [*Auchère et al.*, 2005]. The strongest anisotropies occur during solar maximum as a result of active regions on the solar surface. Moreover, during solar minimum, there can be a $\sim$ 20% reduction in emissions associated with large coronal holes in the polar regions. During the most recent solar minimum (2007–2009), however, there were more large, low-latitude coronal holes and an absence of strong active regions on the solar surface [*Abramenko et al.*, 2010].

[11] Electron-impact ionization, although much weaker than photoionization at 1 AU, does not scale as R^{-2}, and therefore can become important and possibly dominant close to the Sun (<1 AU), where few detailed measurements have been made of solar wind electron distribution functions [*Rucinski and Fahr*, 1989; *McMullin et al.*, 2004]. Consequently, its radial dependence is much less known than the heliospheric, optically thin photoionization, which can be readily scaled from 1 AU observations to other distances as R^{-2}. The electron distributions found in the steady, high-latitude (> 30°) solar winds have been found to be markedly different from those observed at lower latitudes [*Maksimovic et al.*, 2000], leading to lower than expected ionization at high latitudes from the reduced densities and temperatures typically associated with the coronal hole winds.

2.2. He^+ Production Rates

[12] Similar uncertainties exist for the production rates of pickup ions that change on a much shorter time scale. Large variations in solar activity produce changes in the photoionization rate on the time scale of years. However, a sudden coronal mass ejection or solar flare can have an immediate, albeit transient, impact on ionization rates near the Sun [*Rucinski et al.*, 2003]. These transients cause important uncertainties in the determination of the local production of He^+ and have the potential to introduce errors that propagate when combined with models of pickup transport.

2.3. Pickup Ion Velocity Distributions

[13] Numerous analytical and numerical models have been proposed to predict pickup ion transport, and a number of these models have been compared with pickup ion data [e.g., *Vasyliunas and Siscoe*, 1976; *Isenberg*, 1997; *Schwadron*, 1998]. Typically, these models include four key physical processes: (1) upon ionization, newly formed charged particles begin immediately to gyrate about the local magnetic field with a velocity $v = v_{sw}$ in the solar wind frame; (2) ions quickly form a ring distribution; (3) ions preferentially pitch-angle scatter into a shell distribution; and (4) ions cool due to the expanding solar wind and undergo energy scattering, thus reducing their speeds (i.e., $v < v_{sw}$ in the solar wind frame).

[14] Measurements of He^+ combined with forward models have been used to show that ions appear to cool near adiabatically, at least in the outward hemisphere most often observed ($v > v_{sw}$ in the spacecraft frame) [*Saul et al.*, 2009]. The pitch-angle distribution, however, especially during time periods of radial magnetic field, is not isotropic, with particles having difficulty scattering through a pitch-angle of 90°. This difficulty results in pickup ions tending to populate the sunward sectors more than the anti-sunward sectors [*Gloeckler and Geiss*, 1998; *Saul et al.*, 2007]. Although the detailed anisotropic (e.g., with respect to the magnetic field direction) structure of the velocity distributions has not yet been determined, such velocity anisotropies are expected to strongly influence large-scale diffusion and ion transport in the heliosphere [*Möbius et al.*, 1995]. With measurements only of the downwind direction at one heliocentric distance (i.e., 1 AU), potential effects of large-scale diffusion and ion transport cannot be easily characterized.

3. Observations at Solar Minimum

[15] The most recent solar minimum (2007–2009) was a period of unusually quiet and constant solar activity. Overall reduced levels of solar wind mass flux [*McComas et al.*, 2008; *Fisk and Zhao*, 2008] and radiation emission from the Sun [*Woods*, 2010] caused the photoionization and electron-impact ionization rates, respectively, to be uncharacteristically low and nearly constant. Furthermore, the magnetic flux configuration on the Sun is dominated by low-latitude coronal holes and few active regions [*Abramenko et al.*, 2010], which created a more steady-state, nearly spherically symmetric ionization source. Thus, this time period presents a special opportunity for the quantitative study of heliospheric pickup ions.

[16] Here, we use simple models to compute both neutral and ionized helium densities throughout the heliosphere. Although these models take into account the major physical processes that control the densities, there are a number of effects that, for simplicity, will not be considered here. Our modeling efforts are intended only to provide a baseline comparison for the presented spacecraft observations. As we show in this paper, the derived cone properties may be recovered directly from the data without requiring any fitting with neutral models.

3.1. Helium Ionization Rates

[17] The derived EUV photoionization rate [*McMullin et al.*, 2002] during the 2007–2009 period is constant to within approximately 25% of the mean value as shown in Figure 2a. These rates were calculated using measured EUV flux from the Solar Extreme-ultraviolet Monitor (SEM)

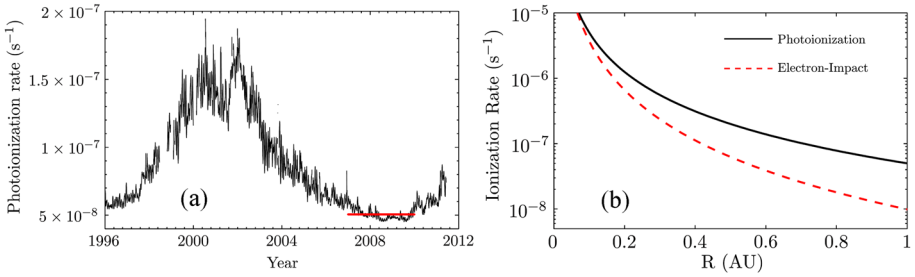

Figure 2. (a) Derived helium photoionization rate at 1 AU following the procedure given by *McMullin et al.* [2002]. During the most recent solar minimum in 2007–2009, the photoionization rate at 1 AU stayed nearly constant at approximately 5×10^{-8} s^{-1}. (b) Radial profiles of photoionization and electron-impact ionization rate following *Rucinski and Fahr* [1989] for the most recent solar minimum. At 1 AU, the electron-impact ionization rate is about 20% of the photoionization rate, but it becomes increasingly more important inside $R = 0.5$ AU.

sensor on the SOlar and Heliospheric Observatory (SOHO), photoionization cross sections from *Samson et al.* [1994], and the solar spectral irradiance from the Whole Heliosphere Interval 2008 Version 2 described by *Woods et al.* [2009]. When compared with the analogous rates used by *Bzowski et al.* [2012], calculated with a different set of measurements and irradiance spectra, there is agreement to within 10%. Despite this good agreement, the absolute uncertainty in these rates may be substantially larger than 10% because of systematic errors in the measurements. Any systematic errors, however, would not alter the near constancy of the measured flux during this time period. An approximately steady-state ionization rate for 2–3 years should result in a nearly steady-state neutral helium distribution within the entire heliosphere.

[18] The *Rucinski and Fahr* [1989] model was used to describe electron-impact ionization with a Maxwell-Boltzmann description of the solar wind electrons and with density and temperature scaling for both core and halo populations. Here, the model input electron densities and temperatures at 1 AU were all reduced by 20% and 10%, respectively, in line with recent observations by Ulysses [*McComas et al.*, 2008; *Fisk and Zhao*, 2008]. Electron temperature radial dependencies are also available from Ulysses observations of polar coronal holes [*Issautier et al.*, 1998; *Maksimovic et al.*, 2000]. However, since our in situ measurements were made close to the Sun, we used the original radial dependencies from *Rucinski and Fahr* [1989] that were derived from observations of electron distribution functions made inside of 1 AU. The radial profile of the calculated electron-impact ionization rate was compared with that of the photoionization rate in Figure 2b. As expected, electron-impact ionization becomes important closest to the Sun, within 0.5 AU. At 1 AU, the electron-impact rate during this time period is approximately 1×10^{-8} s^{-1}, about 20% of the corresponding photoionization rate.

3.2. Neutral Helium Distribution During 2007–2009

[19] Given the large-scale properties of the LISM gas penetrating into the heliosphere, the hot interstellar gas model of *Thomas* [1978] yields the neutral helium density throughout the heliosphere for a steady state spherically symmetric ionization that varies as R^{-2}. As discussed above, the assumptions of steady-state and spherically symmetric ionization are most appropriately applied during this most recent solar minimum, because of the more evenly distributed coronal holes and the absence of active regions on the solar surface. The equations from *Thomas* [1978] were modified with an additional integral as discussed by *Rucinski and Fahr* [1989] to accommodate an arbitrary radial dependence of ionization, thereby enabling the inclusion of electron-impact ionization effects.

[20] In addition to its dependence on R, the neutral density, n, depends on θ, the angle from the upwind direction of the LISM flow (Figure 1). The angle $\theta = 180°$ lies along the cone center. Figure 3a shows the calculated neutral density profiles upwind ($\theta = 0°$) and downwind ($\theta = 180°$) for interstellar parameters from *Möbius et al.* [2004] (model A) and a combination of parameters from *Möbius et al.* [2012] and *Bzowski et al.* [2012] (model B) with and without the inclusion of electron-impact ionization. The corresponding downwind enhancements are shown in Figure 3b. Both sets of interstellar parameters give qualitatively similar density profiles and maximum downwind enhancements. The effect of electron-impact ionization is to push the neutral helium maximum farther from the Sun by about 0.1 AU and reduce the maximum downwind enhancement inside $R = 0.3$ AU.

[21] The absolute neutral density is a strong function of the electron-impact ionization radial profile. However, the range of downwind enhancements at 1 AU (∼8–9) does not appear to be strongly affected by electron-impact ionization, especially when compared with the range of enhancements at $R = 0.3$ AU (∼8–12). For this reason, it is expected that these simple models should match data collected at 1 AU extremely well. The photoionization-only model should provide an upper bound (∼12) on the downwind enhancement at $R = 0.3$ AU since it represents a minimum floor of the ionization state in the heliosphere.

3.3. Pickup Ions as a Proxy for Neutrals

[22] In order to transform these calculated densities into modeled spacecraft observations, a direction of interstellar flow (longitude λ_∞,latitude β_∞) must be assumed. Here, $(\lambda_\infty, \beta_\infty)$ are specified in J2000 ecliptic coordinates. Each point in the heliosphere has a unique triplet (R, λ, β) for which the angular distance (θ) from the inflow direction vector can be calculated from a coordinate frame transformation. For example, for $\beta_\infty = -5.0°$, the MESSENGER and

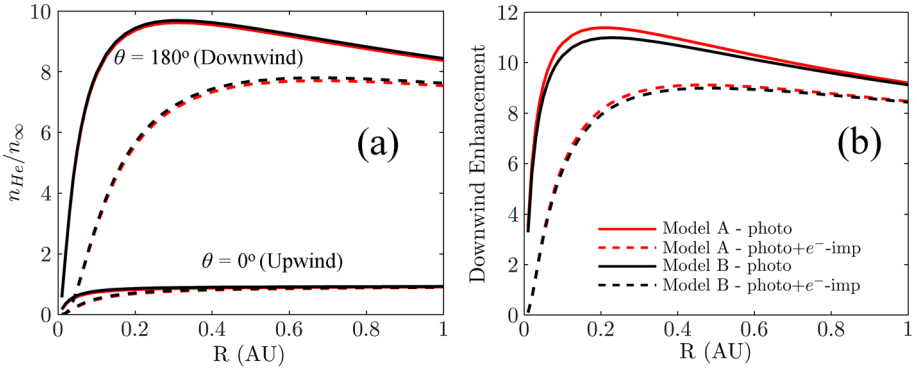

Figure 3. (a) Density distribution of neutral helium as a function of heliocentric distance with the LISM parameters from model A [*Möbius et al.*, 2004] and model B [*Möbius et al.*, 2012; *Bzowski et al.*, 2012] for (top curves) upwind (θ = 0°) and (bottom curves) downwind (θ = 180°) profiles with and without the inclusion of the effects of electron-impact ionization. The strongest enhancement in neutral helium occurs at about R = 0.3 AU. The densities here are normalized by the LISM value, n_∞. (b) The downwind/upwind ratios from Figure 3a as a function of heliocentric distance.

ACE spacecraft orbits do not pass directly through the cone center. Instead, they reach maximum θ values of 171.5° for MESSENGER and 175.0° for ACE, respectively.

[23] The crosswind and upwind densities for $\theta > 90°$ are nearly independent of longitude and consequently should exhibit only radial dependence, such that $n(R,\theta) = n(R)$. Furthermore, from Figure 3, similar downwind enhancements over a given set of radial distances implies that the relative cone structure is nearly independent of R. Under these conditions, the density $n(R,\theta)$ is separable into $n(R)\Theta(\theta)$, where $\Theta(\theta)$ is a dimensionless function that contains the angular structure of the cone. This separation enables the scaling of observed neutral densities to a single heliocentric distance.

[24] MESSENGER/FIPS and ACE/SWICS, however, measure pickup ions, not neutral particles. As detailed in Appendices A and B, a separability of the neutral density $n(R,\theta) \approx n(R)\Theta(\theta)$ translates directly into a separability in measured pickup ion velocity distributions for FIPS and SWICS, i.e., $n_{\mathrm{obs,ion}}(R,\theta) \approx n_o\Theta(\theta)\cdot R^{-\alpha}$, where n_o is a reference density at 1 AU and R is in AU. Under the assumption that this separation is valid, measured pickup ion densities can be used as a proxy for the neutral density distribution in the heliosphere. However, there can be situations in which this separation is not valid.

3.3.1. Transport Effects

[25] Depending on the speed of pitch-angle scattering, there is the possibility of large-scale diffusion and transport of pickup ions due to the average orientation of the heliospheric magnetic field following a Parker spiral configuration. Slow pitch-angle scattering can therefore lead to an offset and spreading of the focusing cone location between the Sun and 1 AU [*Möbius et al.*, 1995]. For such a case, $n_{\mathrm{ion,obs}}$ is no longer separable. However, due to MESSENGER's orbit, the cone transits (i.e., 30° < λ < 120°) are confined between R = 0.3 and 0.4 AU. Observations at R >0.4 AU corresponding to crosswind and upwind longitudes should result in observations of $n_{\mathrm{ion,obs}}$ that are nearly independent of θ regardless of any large-scale diffusion that may be present. The average change in Parker spiral angle between 0.3 and 0.4 AU is only a few degrees. Therefore, even with slow pitch-angle scattering, it is unlikely that any of the transport effects discussed by *Möbius et al.* [1995] could evolve such that they could bias any radial scaling of FIPS observations. There may be, however, time for transport effects to cause differences between the cone structures at R = 0.3 and 1 AU. The manifestation of these effects is examined in section 5.

3.3.2. Solar Wind and IMF Variability

[26] As shown by *Saul et al.* [2003], *Saul et al.* [2007], and *Möbius et al.* [2010], the measured pickup ion density can be distorted through solar wind stream interaction regions and the orientation of the interplanetary magnetic field. These distortions are statistically independent of ecliptic longitude because they are caused by solar rotation. Furthermore, the timescale of these variations is much shorter than the evolution of the neutral density distribution in the heliosphere during solar minimum. Consequently, there should not be a strong observed longitudinal signature in pickup ion measurements due to solar wind variability.

3.3.3. Sensor Field of View

[27] ACE/SWICS has a nearly stationary field of view (integrated over a spacecraft spin and energy scanning period of 12 min) and therefore samples a nearly constant section of the pickup ion distribution function. MESSENGER/FIPS, however, has a more dynamic orientation due to spacecraft maneuvering. In order to protect the spacecraft and its instruments, MESSENGER has a large sunshade pointed in the solar direction. The FIPS sensor aperture points out of the side of the spacecraft, imaging nearly 1.4π sr about its boresight direction. The sensor is capable of viewing particles entering within ±15° of the spacecraft R direction in the radial-tangential-normal (RTN) coordinate system [*Gershman et al.*, 2012]. With the sunshade always directed toward the Sun, the spacecraft is free to roll about the R-axis, such that the FIPS orientation can be approximated by a vector in the T-N plane. As the spacecraft rolls, different sections of the pickup ion distribution become visible. These rotations are, in principle, independent of ecliptic longitude. Therefore, variations in the FIPS field of view (FOV) should not contribute to any apparent longitudinal structure in pickup ion measurements.

However, the spacecraft orientation as a function of time is examined in section 4.1 to determine any potential bias due to a finite number of maneuvers. During 2007–2009, MESSENGER performed approximately 40 rotations about the spacecraft *R*-axis.

[28] Under the aforementioned assumptions, all FIPS measured $n_{obs,ion}$ values can be scaled to remove any dependence on the radial distance *R* of MESSENGER spacecraft from the Sun. This scaling enables the recovery of the relative neutral cone structure from a set of pickup helium observations at different heliocentric distances.

4. He^+ Measurements

[29] The data analysis here consists of double-coincidence measurements from two spaceborne time-of-flight (TOF) mass spectrometer sensors, MESSENGER/FIPS ($0.3 < R < 0.7$ AU), and ACE/SWICS ($R \sim 1$ AU). ACE/SWICS is nominally a triple-coincidence sensor that measures the energy per charge, mass per charge, and energy of incident ions and has been described in detail by *Gloeckler et al.* [1998]. However, the observations from ACE/SWICS used here are derived using a double-coincidence data product recently developed by *Gilbert et al.* [2012], as He^+ can be easily resolved from other species without the need for a solid-state detector that is required to determine charge state composition of the solar wind.

[30] FIPS, with its novel electrostatic analyzer (ESA) geometry, simultaneously images particles in three-dimensional velocity space over $\sim 1.4\pi$ sr about its boresight direction. The entrance directions of these particles map onto an imaging detector, providing an angular resolution accurate to within approximately 15°. In its interplanetary cruise mode of operation, the ESA scanned through 60 logarithmically spaced energy steps between 0.05 and 10 keV/e in 64 s. The TOF of these ions was measured, deriving a mass per charge estimate up to 40 amu/e. The details of the FIPS sensor have been documented in further detail by *Andrews et al.* [2007]. Unlike SWICS, FIPS, because of imposed mass and power constraints, does not have triple-coincidence capabilities. Although the absence of energy measurements limits analyses with respect to solar wind ions [*Gershman et al.*, 2012], He^+ is well-resolved from only double-coincidence TOF measurements.

[31] For each spacecraft, the phase space distribution of measured He^+ events as a function of incident speed, $f(v)$, was computed using the number of measured events as a function of incident speed, $N(v)$, from the relation $f(v) \sim N(v)/v^4$ [*von Steiger et al.*, 2000; *Raines et al.*, 2011; *Gershman et al.*, 2012]. Multiplicative factors such as the instrument's geometric factor and energy resolution that are not discussed in detail here ensure proper unit conversion between $f(v)$ and $N(v)$. This distribution was then integrated according to equation (1) to generate observed densities as a function of time,

$$n_{obs,He+} = \int v^2 f(v) \mathrm{d}v. \quad (1)$$

[32] The observed density, $n_{obs,He+}$, is computed from individually measured He^+ events, independent of any estimation of solar wind speed or the structure of the pickup ion distribution function. This density corresponds to the fraction of the He^+ distribution that is visible to a sensor and is, in general, dependent on the sensor's angular FOV and energy response. As discussed in detail in section 3.3 and Appendices A and B, $n_{obs,He+}$ may exhibit apparent structure due to changes in solar wind conditions or sensor orientation.

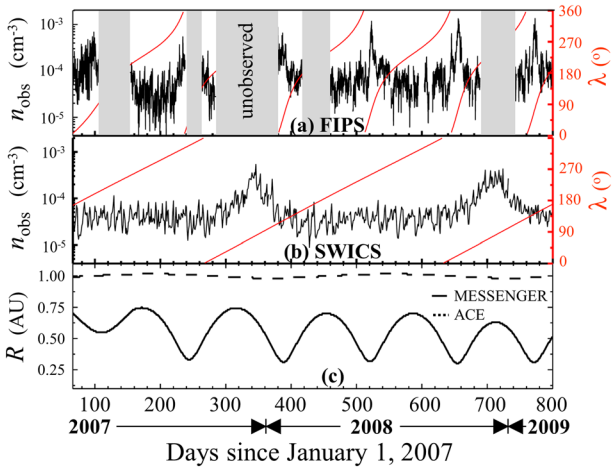

Figure 4. Unscaled measurements of He^+ during 2007–2009 for (a) MESSENGER/FIPS and (b) ACE/SWICS. In each panel the variation of the ecliptic longitude (λ) with time is also shown in red. (c) The radial distance from the Sun of each spacecraft is indicated here. An enhancement was clearly observed near the predicted downwind direction ($\approx 75°$) at all distances, with MESSENGER having passed through the cone once near $R = 0.6$ AU, and then several times at $R = 0.3$ AU, and ACE passing through the cone yearly at $R = 1$ AU. The daily count on the horizontal axis begins on 1 January 2007.

4.1. Data Overview

[33] During 2007–2009, MESSENGER passed through the gravitational focusing cone once at $R \approx 0.6$ AU and at least three times at $R \approx 0.3$ AU. A time series of unscaled He^+ measurements from MESSENGER/FIPS and ACE/SWICS during this time period is shown in Figure 4. FIPS and SWICS data have been time-averaged in 4 h and daily intervals, respectively. In each pass, a clear enhancement in observed He^+ is apparent near the downwind direction, i.e., $\lambda \approx 75°$. Similar enhancements occur when ACE passed through the cone at 1 AU in late November to early December of 2007 and 2008. The He^+ densities observed by FIPS also changed with MESSENGER's radial variation in its heliocentric orbit. However, enhancements at both $R \approx 0.6$ and $R \approx 0.3$ AU indicate that increased He^+ flux measured by FIPS is a result of the spacecraft passing through the cone rather than a change in heliocentric distance. Data collected by MESSENGER/FIPS before 21 September 2007 (day 264, for a day number count that begins with 1 January 2007) relied on a version of the instrument flight software that limits our analysis and its comparisons to the data collected later. Therefore, our detailed analysis of MESSENGER/FIPS observations is necessarily restricted to those collected after 21 September 2007.

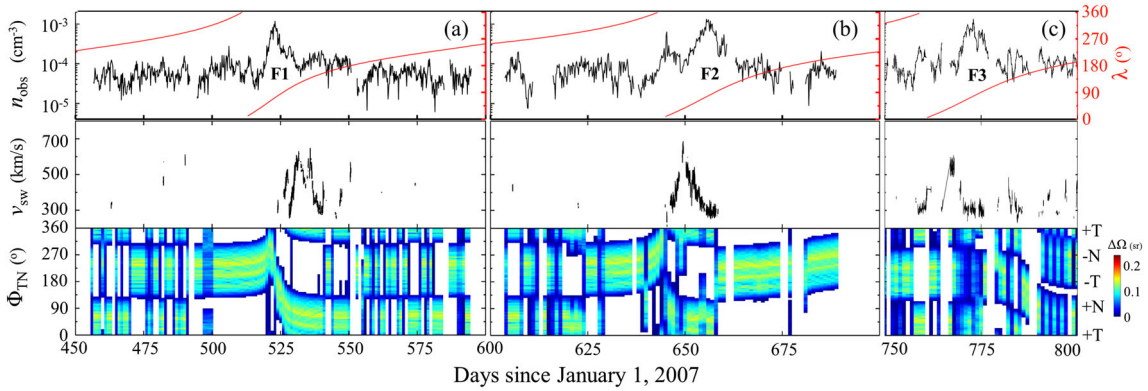

Figure 5. A detailed look at three transits of MESSENGER through the helium focusing cone: (a) F1, (b) F2, and (c) F3. The unscaled observed densities from FIPS and ecliptic longitude λ of MESSENGER are shown in the top panel, the available FIPS-observed solar wind speeds are shown in the middle panel, and the FIPS visibility as a function of clock angle in the *T*-*N* plane, Φ_{TN}, is shown in the bottom panel. Enhancements in the He^+ flux were observed at the transitions from high-speed to low-speed solar wind streams. Some changes in the He^+ flux were also observed during changes in spacecraft orientation. The daily count on the horizontal axis begins on 1 January 2007.

We further restrict our analysis to the three cycles of the FIPS data after day number 450, since each individual cycle contains observations that span a nearly complete range of ecliptic longitudes.

[34] A closer look at the individual cone transits for MESSENGER (here termed as F1, F2, and F3) and ACE (termed S1 and S2) is shown in Figures 5 and 6, respectively. Each figure includes available solar wind speeds measured by FIPS on MESSENGER, and SWEPAM on ACE. In Figure 5, the FOV of FIPS is also included. Here, Φ_{TN} defines a clock angle in the *T*-*N* plane, and $\Phi_{TN} = 0$ corresponds to the $+T$ direction. Although the FIPS FOV does extend out of the *T*-*N* plane, the view direction of each pixel in the FIPS FOV can be projected onto a particular Φ_{TN} angle. The solid angle ($\Delta\Omega$) in each pixel is accumulated into the appropriate $5°\Phi_{TN}$ bin, providing a visualization of the sensor orientation and FOV as a function of time, such that the sum ($\Delta\Omega$) in each scan equals the FIPS total visible solid angle of $\sim 1.4\pi$ sr.

[35] The orientation of FIPS changed often within all ecliptic longitude regions (i.e., downwind, crosswind, and upwind), even within a single cone transit. From examination of Figure 5, changes in observed He^+ densities appear to have been affected by changes in solar wind speed as well as by changes in the FIPS FOV, although without a more complete set of solar wind observations, it is difficult to quantify which factor was a more important influence.

[36] As discussed in detail by *Gershman et al.* [2012], solar wind particles are nominally obstructed from the FIPS FOV by the spacecraft sunshade. These particles can nonetheless be measured during times of sufficient aberration due to the spacecraft $+T$ component of velocity around the Sun, but only if the sensor is oriented properly. As shown in Figure 5, solar wind speeds from FIPS are available only

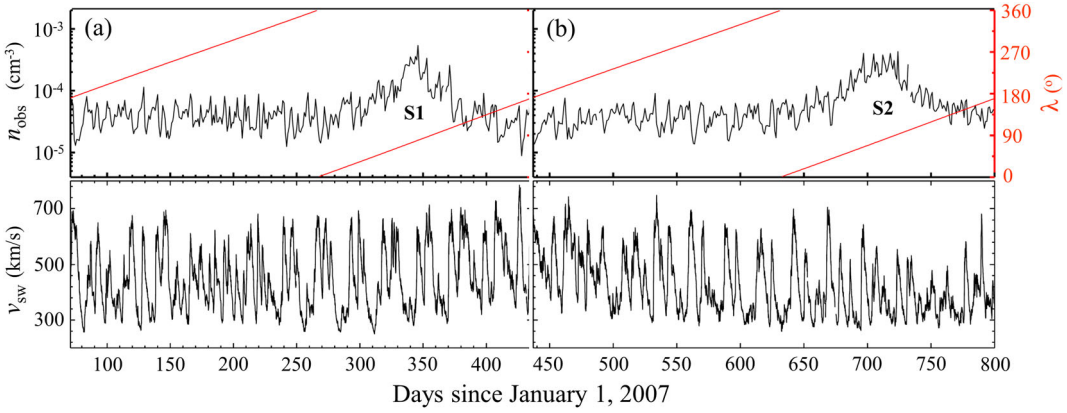

Figure 6. A detailed look at two transits of ACE through the helium focusing cone: (a) S1 and (b) S2. The observed densities from SWICS and ecliptic longitude λ of ACE are shown in the top panel, and the available ACE/SWEPAM-observed solar wind speeds are shown in the bottom panel. Enhancements in the He^+ flux were observed at the transitions from high-speed to low-speed solar wind streams. The daily count on the horizontal axis begins on 1 January 2007.

when $\Phi_{TN} \approx 0$ was visible, i.e., the $+T$ direction. MESSENGER reached its maximum speed of $\approx$ 60 km/s closest to the Sun. It was during these time periods that the aberration effect became sufficiently strong to enable the recovery of solar wind speeds from FIPS observations. During time periods when the spacecraft speed was small (i.e., $R > 0.5$ AU), solar wind speeds are not available, even with ideal sensor orientation.

4.2. Radial Scaling of FIPS Measurements

[37] Before analyzing the structure of the focusing cone in the inner heliosphere, the MESSENGER/FIPS observations of $n_{obs,He+}$ must be scaled to $R = 0.3$ AU by a factor R^{α} in order to remove effects due to the radial variation of the spacecraft's orbit. Such a scaling is not required for ACE/SWICS observations. Here, we use the fact that observations of He^+ in the upwind directions should vary only with heliocentric distance. For a downwind direction near $\lambda = 75°$, the upwind longitudes are defined as $165° < \lambda < 345°$. Observations made within this range of λ values were accumulated into 5°-wide λ bins, averaging over the density variations measured at a particular ecliptic longitude mentioned in section 3.3. This resulting distribution was then divided by its average density value to form a set of normalized upwind densities as a function of λ, $\hat{n}_{uw}(\lambda)$.

[38] As shown in Figure 4, the maximum radial distance of MESSENGER from the Sun consistently occurred near $\lambda = 230°$, well within the range of the upwind longitudes. Consider the effect of scaling FIPS measurements of $n_{obs,He+}$ by a factor of R^{α}. If α is set to be too low (underscaling), then there will be an observed depression in $\hat{n}_{uw}(\lambda)$ at $\lambda = 230°$. If α is set to be too high (over scaling), then there will be an enhancement at $\lambda = 230°$. The proper scaling exponent α, therefore, can be determined by finding the value that results in the flattest $\hat{n}_{uw}(\lambda)$ distribution. The functional form of $\hat{n}_{uw}(\lambda)$ can be approximated by a parabola $a(\lambda - 230°)^2 + c$, with c set so that the average value of $\hat{n}_{uw}(\lambda)$ is equal to 1. Here, a is a free parameter fit to a given $\hat{n}_{uw}(\lambda)$ distribution: $a > 0$, $a < 0$, and $a = 0$ indicate overscaling, underscaling, and proper scaling, respectively.

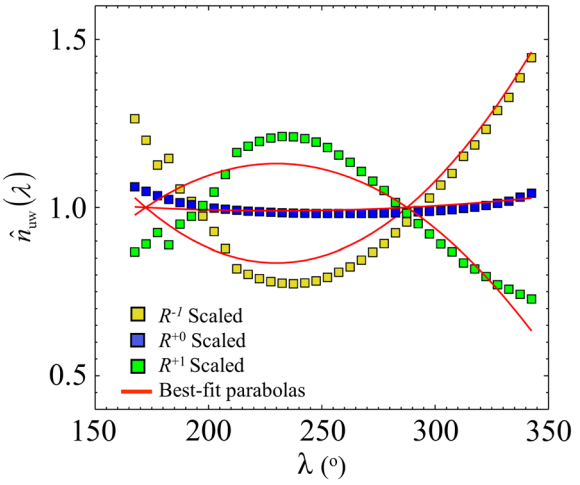

Figure 7. Radially scaled $\hat{n}_{uw}(\lambda)$ distributions for the MESSENGER spacecraft trajectory and neutral densities at $R = 0.3$ AU from model B [*Möbius et al.*, 2012; *Bzowski et al.*, 2012] including the effects of electron-impact ionization. Best-fit parabolas of the form $a(\lambda - 230°)^2 + c$, are shown for the R^{-1} (underscaling), R^0 (proper scaling), and R^{+1} (overscaling) cases. The R^0 case has the parabola with the smallest value of a although still exhibits some curvature, resulting in errors in the recovered ideal scaling exponent on the order of 0.1.

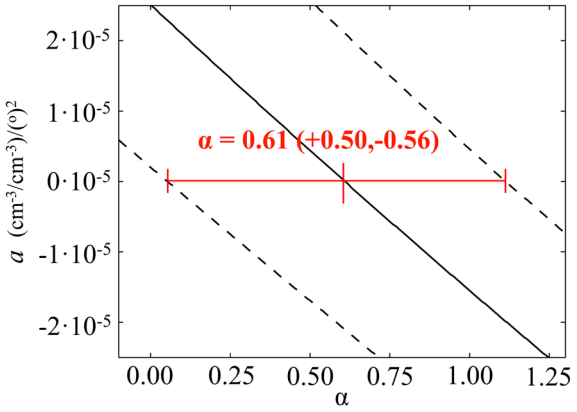

Figure 8. Best-fit a values from fitting a parabola of the form $a(\lambda - 230°)^2 + c$ to measured FIPS $\hat{n}_{uw}(\lambda)$ distribution as a function of radial scaling exponent α (solid line). Values of a that result in RMS errors of the parabolic fit within 5% of the minimum are also included (dashed lines). The value of α that results in the flattest $\hat{n}_{uw}(\lambda)$ distribution is $\alpha = 0.61(+0.50, -0.56)$.

[39] We can test this approximation for $\hat{n}_{uw}(\lambda)$ by using the modeled neutral distributions from section 3.2 and knowledge of MESSENGER's orbit. As an example, we assume that the helium neutral density is defined by the interstellar flow parameters of model B including the effects of electron-impact ionization. For the full range of times in Figure 5, the angular distance of the spacecraft from the assumed downwind direction is calculated. The corresponding n_{He} is then sampled from the modeled $R = 0.3$ AU cone, regardless of spacecraft heliocentric distance. Therefore, the synthetic data are prescaled to the same heliocentric distance. The simulated upwind observations were scaled by a factor R^{α} to form $\hat{n}_{uw}(\lambda)$ for $\alpha = +1$ (overscaling), $\alpha = 0$ (proper scaling), and $\alpha = -1$ (underscaling). Best-fit, i.e., minimized root-mean-squared (RMS) error, parabolas are shown along with each curve in Figure 7 and illustrate the change of inflection when the data are scaled by different values. Here, the precise match of the fits to the data are less important than capturing relative changes in curvature. Of the three, $\alpha = 0$ results in the flattest $\hat{n}_{uw}(\lambda)$, and overscaled and underscaled values lead to enhancements and depressions in the upwind data at $\lambda = 230°$, respectively. However, the $\alpha = 0$ curve has a slight upward inflection such that the sampled modeled upwind data do not create a perfectly flat $\hat{n}_{uw}(\lambda)$ distribution. This curvature is expected to result in errors in the determination of α on the order of 0.1.

[40] This scaling process can next be applied to the measured FIPS upwind data. Figure 8 shows the best-fit values of a for each radial scaling exponent α between 0 and 1.25. We define the uncertainty of the fits by values of a that result in RMS errors within 5% of the minimum error, resulting in the

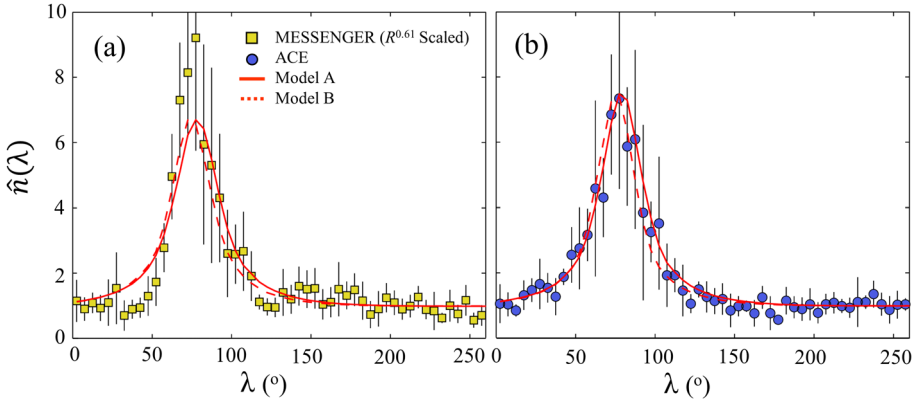

Figure 9. Average structure of the helium gravitational focusing cone from (a) MESSENGER/FIPS (R = 0.3 AU) and (b) ACE/SWICS (1 AU). Error bars indicate the standard deviation of densities accumulated in each 5° interval. Structure from neutral models with LISM parameters from model A [*Möbius et al.*, 2004] and model B [*Möbius et al.*, 2012; *Bzowski et al.*, 2012] including the effects of electron-impact ionization, is shown by the solid and dashed red lines, respectively. The similarity in derived cone centers at R = 0.3 AU and R = 1 AU indicates that there is no substantial ion transport or diffusion between the two radial distances.

lower and upper dashed lines in Figure 8. The best-fit radial scaling exponent for MESSENGER/FIPS data is found to be α = 0.61, with upper and lower bounds of α = 1.11 and α = 0.05, respectively.

4.3. He Focusing Cone Structures

[41] With the MESSENGER data radially scaled, the recovery of the cone structure is possible for heliocentric distances R = 0.3 AU and R = 1 AU. The quantities that best describe the cone are its width, its relative downwind enhancement with respect to the upwind observations, and its center location in ecliptic longitude. These quantities were calculated for each individual cone transit for both MESSENGER (F1,F2, and F3) and ACE (S1 and S2) and then all transits were combined to form a set of averaged solar minimum focusing cones for each spacecraft.

[42] The width of each cone transit for the two spacecraft can be calculated directly from the density profile of the cone, $\hat{n}(\lambda)$. $\hat{n}(\lambda)$ was found by a process identical to that used to determine the upwind density distribution $\hat{n}_{uw}(\lambda)$, but for the full set of ecliptic longitudes. As an example, the averaged scaled FIPS and SWICS $\hat{n}(\lambda)$ distributions are shown in Figure 9 along with the modeled distributions (A and B) that include the effects of electron-impact ionization. The error bars indicate the standard deviation of density observations in each 5° λ bin. The modeled data provide an excellent match to the observations, especially at 1 AU where the effects of electron-impact ionization are not expected to have a strong impact on the relative cone structure, as discussed in Section 3.2.

[43] The $\hat{n}(\lambda)$ distributions were interpolated to bins of 1° and then the maximum value, the full width half maximum (FWHM), and the average of the FWHM leading and trailing longitudes were computed, providing estimates of the downwind enhancement, cone width, and cone center, respectively. The quantities calculated from both FIPS and SWICS measurements are summarized in Tables 1 and 2. Quantities derived from the neutral density models were generated from the trajectories of both MESSENGER and ACE. As shown in Tables 1 and 2, the computed cone centers for the modeled data calculated with this method are accurate to within about 1°. For FIPS, the uncertainties in the recovered cone parameters from the uncertainties in α, which primarily affect the recovered downwind enhancement. The downwind enhancements, cone centers, and widths from SWICS match the model predictions well, especially for the average transit case. From FIPS, the observed widths are small and the downwind enhancement is large compared with both the SWICS measurements and modeled distributions. This enhancement is large even when compared with the photoionization-only case, which should represent an upper bound on the downwind neutral density enhancement.

Table 1. Focusing Cone Parameters Recovered From FIPS Observations[a]

	Measured Observations				Modeled Observations			
	F1	F2	F3	Average	A	A (e^-)	B	B (e^-)
λ_∞	71.0°	79.0°	78.5°	76.0°	74.5°	74.5°	78.0°	78.0°
Enhancement	9.8(+4.2, –2.6)	11.8(+4.4, –3.0)	8.3(+2.1, –1.6)	9.1(+3.5, –2.3)	8.3	6.7	8.2	6.7
FWHM	20°	26°	31°	29°	35°	35°	38°	38°

[a]Results for individual transits (F1, F2, and F3) are shown along with data averaged over all three cone passes. Parameters are also given for modeled observations averaged over all passes using either model A or model B; models that include the effects of electron-impact ionization are denoted by (e^-).

Table 2. Focusing Cone Parameters Recovered From SWICS Observations[a]

	Measured Observations			Modeled Observations			
	S1	S2	Average	A	A (e^-)	B	B (e^-)
λ_∞	77.5°	77.0°	77.0°	75.0°	75.0°	79.0°	79.0°
Enhancement	8.5	8.0	7.3	8.0	7.4	7.9	7.4
FWHM	19°	38°	34°	32°	32°	36°	36°

[a]Results for individual transits (S1 and S2) are shown along with data averaged over both cone passes. Parameters are also given for modeled observations averaged over both passes using model A or model B; models that include the effects of electron-impact ionization are denoted by (e^-).

[44] The differences between cone properties for individual transits are likely due to the interplay between the time duration of each spacecraft cone transit and the average timescale of changes in solar wind speed. The ACE spacecraft orbits around the Sun at approximately 1°/day. From the widths in Table 2, each ACE focusing cone traversal therefore lasts 20–40 days, on the order of a Carrington rotation. During this time interval, the SWICS He^+ measurements span several high-speed and lower-speed streams. The leading and trailing edges (1–2 days each) of the focusing cone last less than the overall cone transit (20–40 days), so their determination is sensitive to the changing solar wind conditions. This sensitivity results in differences in the calculated cone width for each pass. The measured downwind enhancement, however, is less sensitive to these variations, since its value is calculated using data averaged over several days.

[45] MESSENGER, however, near the downwind direction, orbits the Sun at approximately 6°/day. Each cone transit can potentially occur during only a single solar wind stream. In the case of F2 and F3, for example, during which solar wind conditions are known, the majority of the transit occurred directly after the transition from a fast to slow wind stream. From *Saul et al.* [2003], *Saul et al.* [2007], *Möbius et al.* [2010], and an examination of the correlation between solar wind speed and He^+ densities observed by SWICS in Figure 6, these regions often result in enhancements in the observed He^+ density. Such enhancements could result in lower cone widths and higher downwind/upwind density ratios. The cone center, however, remains unchanged by such an effect, as evidenced by similar derived centers determined for both the F2 and F3 transits. The FIPS orientation during both of these transits appears to have been nearly symmetric and is unlikely to have caused a substantial bias in the calculation of the FWHM and cone center longitude.

[46] The cone center from F1 is much lower in ecliptic longitude than all other passes from either MESSENGER or ACE. Although solar wind speeds are not available for the full F1 transit, a quick transition from high- to low-speed wind around day number 530 appears correlated with an enhancement in observed He^+, resulting in a lower value of the trailing λ value used in the FWHM calculation, and consequently a possible underestimation of both the FWHM and longitude of cone center. Furthermore, the FIPS orientation was asymmetric during this pass, and could therefore create a bias to the determination of the leading and trailing longitudes of the FWHM.

5. Discussion

[47] From pickup ion data alone it is difficult to tightly constrain the interstellar flow direction, even under the simplest conditions at solar minimum. This difficulty is due to a number of processes taking place that affect neutral helium particles entering the heliosphere and the dynamics and transport of pickup ions. The time dependence of these processes becomes even more complex at solar maximum. However, a relatively wide cone enables analysis of each pass using many data points. From these analyses, independent of the radial scaling of FIPS data, the MESSENGER/FIPS and ACE/SWICS data indicate an average λ_∞ of 76.0°(±6.0°) and 77.0°(±1.5°), respectively.

[48] The uncertainties in the cone center direction are derived from the maximum angular distance of the individually computed values to the average value, with an additional 1° included to take into account error in the inversion process. These recovered interstellar flow directions, especially from the MESSENGER F2 and F3 transits, are closer to the recent IBEX results than previous determinations from pickup ion data during solar maximum [*Gloeckler et al.*, 2004]. However, the recovered λ_∞ values are also within the uncertainties given by *Möbius et al.* [2004].

[49] Given the tight constraints on v_∞ and T_∞, errors in the modeled neutral cone structure are primarily a function of the uncertainty in the helium ionization rates. Large variations in the predicted downwind enhancement at $R = 0.3$ AU with different neutral models from section 3 indicate that the cone structure in the inner heliosphere is extremely sensitive to the effects of electron-impact ionization. Conversely, it is difficult to use the pickup ion observations at 1 AU with ACE/SWICS to resolve such effects. Further analysis of MESSENGER/FIPS measured distribution functions may help to constrain these ionization profiles.

[50] The good agreement between the λ_∞ values derived from the MESSENGER/FIPS data scaled to $R = 0.3$ AU and the ACE/SWICS data at 1 AU indicates that any large-scale ion transport or diffusion between these two radial distances is tightly constrained. From *Möbius et al.* [1995], any offset due to diffusive transport should be accompanied by an increase in cone width and reduction in downwind enhancement when compared with the predicted neutral density. Neither effect is observed outside the uncertainties of the recovered cone parameters. These constraints imply that the pitch-angle scattering of He^+ pickup ions does not create any marked longitudinal streaming.

6. Concluding Remarks

[51] This most recent solar minimum has provided an unprecedented opportunity for the study of the interstellar helium distribution in the heliosphere. The expected ionization rates of neutral particles were not only at an all-time low, but they also reached a nearly steady state. This unusually quiet period of solar activity enabled the averaging of spacecraft data over long time periods, providing a robust delineation of cone structure. With data averaged over this most recent solar minimum, the structure of the helium gravitational focusing cone has been mapped at multiple heliocentric distances for the first time from in situ measurements of pickup ions. Radial-distance-scaled MESSENGER/FIPS observations combined with data from ACE/SWICS during

the same time period led to the delineation of the cone structure at R = 0.3 and 1 AU with downwind enhancements of ≈ 8 and widths of ≈ 30°. Comparisons with models of the neutral density yielded good matches with established LISM parameters and λ_∞ = 76.0°(±6.0°) and 77.0°(±1.5°) for R = 0.3 AU and 1 AU, respectively. The lack of any substantial differences in the cone structure between those solar distances during this time period implies that measurements at 1 AU are a surprisingly sensitive and useful tool for mapping the distribution of neutral helium in the ecliptic. However, measurements inside of 0.5 AU may be required to best understand the effects of electron-impact ionization. These data do not require the presence of any secondary neutral helium population in the heliosphere to explain their variations. Through its nominal and extended mission in orbit around Mercury, MESSENGER will continue to provide observations of He^+ in the inner heliosphere that can be compared with data collected near-Earth.

Appendix A: Instrument Response Functions

[52] In addition to observing pickup ions at different heliocentric distances, FIPS and SWICS have markedly different fields of view and, consequently, analyze different sections of the pickup ion velocity distribution function, as illustrated in Figure A1.

[53] As discussed in section 2.3, the pickup ion distribution is organized in the solar wind rest frame, not the spacecraft/instrument frame. Particle velocities relative to the center of this frame are typically normalized by the solar wind speed, v_{sw}, i.e., they can be described by the vector $\mathbf{w} \equiv \mathbf{v}/v_{sw}$. Previous pickup ion observations indicate that the velocity distribution exhibits structure with respect to the anti-sunward and sunward directions, i.e., particles move both faster and slower than the solar wind, respectively, in the instrument frame.

[54] ACE/SWICS, a solar wind monitor, continuously measures solar wind plasmas. The sensor FOV points nearly radially, with a slight angle that evolves slowly as a function of time (dubbed the "aspect angle") due to spacecraft orientation. In data processing, the steps in energy per charge near the solar wind values are excluded to ensure that high fluxes of solar wind H^+ or He^{2+} particles do not contaminate the time-of-flight track of pickup He^+ and that no He^+ of solar origin is included. These restrictions set a processing threshold of $|\mathbf{w}| > 0.2$ in the anti-sunward sector for all ACE/SWICS data analysis of He^+ used here, i.e., particles measured by the instrument with speeds greater than 1.2 times the solar wind speed. Due to ACE's near circular orbit around the Sun (i.e., at Earth's L1 point) and constant pointing, the SWICS view of the pickup ion distribution is approximately constant over time, although there are some slight variations with solar wind speed.

[55] MESSENGER is intended to study the planet Mercury, with FIPS's direct view of the Sun masked by a large spacecraft sunshade. Due to this physical obstruction, FIPS cannot view particles with $|\mathbf{w}| < 0.5$. Furthermore, particles measured with ratios of energy per charge less than 500 eV/e were excluded because of low signal-to-noise ratios at those values. As shown in Figure A1, FIPS mostly views the sunward sector. Although the instantaneous field of view is not symmetric about the radial direction, to first order the spacecraft maneuvers are symmetric about the spacecraft—Sun line. As discussed and illustrated in section 4.1, as the spacecraft changes orientation in flight, different sections of the distribution function are sampled. The spacecraft rolled approximately 40 times during cruise, so that much of the sunward sector was measured at multiple heliocentric radii and heliographic longitudes.

[56] These measurement constraints can be represented mathematically by an instrument response function, D, a factor that describes the fraction of the distribution visible to a sensor. Note that D is not used in the calculation of n_{obs,He^+} in section 4 and is used here only to provide an understanding of the effect of sensor orientation and FOV on the measured n_{obs,He^+} values. In general, D is a three-dimensional function. However, as a simplification, D is discussed as $D(|\mathbf{w}|)$, a function of only the speed in the solar wind frame in a particular sector. For SWICS, D models visibility in the anti-sunward sector for $|\mathbf{w}| > 0.2$. For FIPS, D is primarily a function of $|\mathbf{w}| > 0.5$ in the sunward sector, as shown in Figure A2. Here, $D(|\mathbf{w}|)$ was determined through the sampling of a set of spherical shell velocity distributions within an example FIPS FOV (12 February 2009, 00:00:35 UTC), illustrated in Figure A2a in standard RTN spherical coordinates (θ_{RTN}, Φ_{RTN}). Here, θ_{RTN} is the angle from the N axis and Φ_{RTN} is the clock angle in the R–T plane with the Sun visible at (θ_{RTN} = 90°, Φ_{RTN} = 0°). The FIPS FOV nominally extends from 15° to 75° away from its boresight vector in all directions. However, the spacecraft body and solar panel arrays create additional obstructions projected onto the FIPS FOV.

[57] For each visible (θ_{RTN}, Φ_{RTN}) value, the phase space density of a spherical shell distribution centered on a constant $|\mathbf{w}|$ with width $0.05|\mathbf{w}|$ was sampled for the energy range 500 eV/e–10 keV/e. Two solar wind speed cases of v_{sw} = 400 and 600 km/s were used. The observed densities in both the sunward and anti-sunward sectors were determined and normalized by the total densities of the distribution in each hemisphere, resulting in $D(|\mathbf{w}|)$, shown in Figure A2b. In this simplified model, the phase space density was sampled directly, and not converted into a finite number of instrument-measured events.

[58] For both fast and slow solar wind speeds, approximately 30% of the sunward sector is visible to FIPS for $|\mathbf{w}| > 0.5$, with substantially less of the distribution visible in the anti-sunward sector. Most of the pickup ions are expected to be measured for $|\mathbf{w}| < 1$ since newly picked up ions have $|\mathbf{w}| \approx 1$ in the solar wind frame and cool to smaller $|\mathbf{w}|$-values as they are convected out into the heliosphere in the expanding solar wind. This cooling creates an effective mapping between the ions picked up at a particular heliocentric distance, R_{pickup}, and the $|\mathbf{w}|$-value in the pickup ion velocity distribution. For adiabatic cooling, this mapping is $R_{pickup} = R|\mathbf{w}|^{3/2}$ [*Vasyliunas and Siscoe*, 1976]. With a $|\mathbf{w}| > 0.5$ restriction for FIPS and a $|\mathbf{w}| > 0.2$ restriction for SWICS, given their minimum heliocentric distances of 0.3 and 1 AU, respectively, neither instrument is expected to be sensitive to any ions produced inside R = 0.1 AU.

Appendix B: Pickup Ion Densities

[59] The total pickup ion density as a function of the neutral density and ionization rate is,

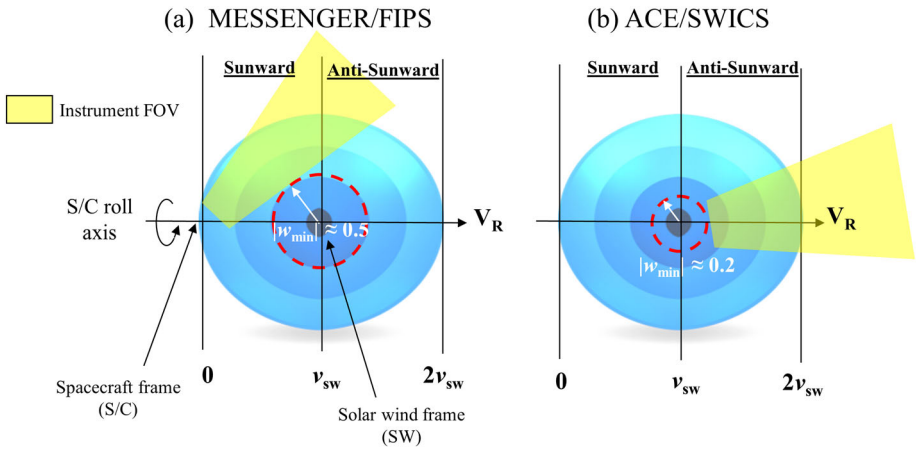

Figure A1. Instrument field of view of a pickup ion distribution centered on the solar wind frame for (a) MESSENGER/FIPS and (b) ACE/SWICS. FIPS primarily views the sunward sector of the distribution; given the spacecraft (S/C) roll-axis, i.e., the spacecraft—Sun line, other sections of the distribution are sampled as the spacecraft rolls during flight. A smaller portion of the anti-sunward sector is visible to FIPS. ACE/SWICS has a view restricted to the anti-sunward sector, slightly offset from the radial direction by the spacecraft aspect angle. The dashed circle indicates the minimum observable velocity relative to the solar wind core that can be measured by each instrument.

$$n_{\mathrm{ion}}(R,\theta) = \frac{1}{R^2}\int_{R_{\mathrm{SUN}}}^{R} \mathrm{d}R' \cdot \frac{R'^2\beta(R')n(R',\theta)}{v_{\mathrm{sw}}}, \tag{B1}$$

where R_{SUN} is the radius of the Sun, β is the local production (i.e., ionization) rate of He^+, and v_{sw} is the solar wind speed. The instrumentally observed density, $n_{\mathrm{obs,ion}}$, will be similar to the density from equation (B1) but with the production rates convolved with the instrument response function D, such that,

$$n_{\mathrm{obs,ion}}(R,\theta) = \frac{1}{R^2}\int_{R_{\mathrm{SUN}}}^{R} \mathrm{d}R' \cdot D(|\mathbf{w}|) \cdot \frac{R'^2\beta(R')n(R',\theta)}{v_{\mathrm{sw}}}. \tag{B2}$$

[60] Following the discussion in section 3.2, for radial distances with similar cone structure, i.e., constant downwind/upwind ratios, $n(R,\theta) \approx n(R)\Theta(\theta)$. We also note that D is a function only of R, under the assumption that some kind of mapping between $|\mathbf{w}|$ and R exists. For this case,

$$n_{\mathrm{obs,ion}}(R,\theta) \approx \frac{1}{R^2}\int_{R_{\mathrm{SUN}}}^{R} \mathrm{d}R' \cdot D(|\mathbf{w}|) \cdot \frac{R'^2\beta(R')n(R')\Theta(\theta)}{v_{\mathrm{sw}}} \approx \Theta(\theta)g(R), \tag{B3}$$

where

$$g(R) \equiv \frac{1}{R^2}\int_{R_{\mathrm{SUN}}}^{R} \mathrm{d}R' \cdot D(|\mathbf{w}|) \cdot \frac{R'^2\beta(R')n(R')}{v_{\mathrm{sw}}}. \tag{B4}$$

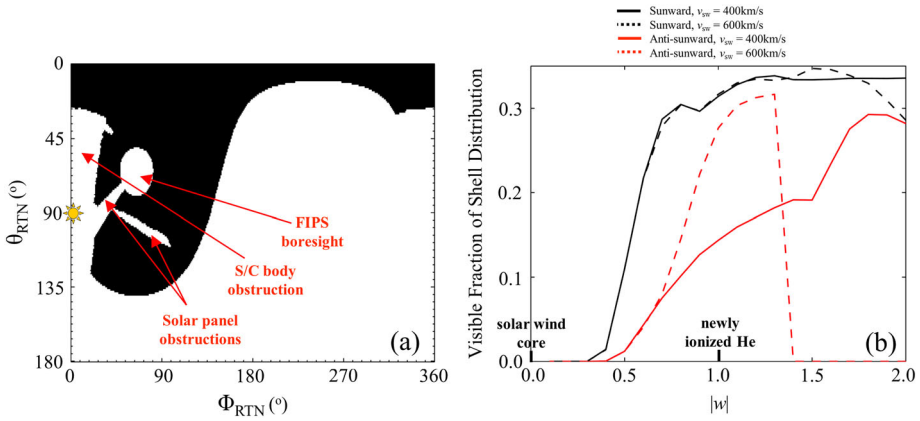

Figure A2. (a) FIPS FOV on 12 February 2009 at 00:00:35 UTC, as a function of (θ_{RTN}, Φ_{RTN}), where ($\theta_{\mathrm{RTN}} = 90°$, $\Phi_{\mathrm{RTN}} = 0°$) corresponds to the solar direction. The black pixels represent directions visible to the sensor. Obstructions to the FIPS FOV due to the spacecraft body and solar panel arrays are also indicated. (b) $D(|\mathbf{w}|)$, i.e., the visible fraction of the sampled shell distributions using the FOV in Figure A2a, in both the sunward and anti-sunward hemispheres for solar wind speeds of 400 and 600 km/s. Newly ionized helium particles are injected into the distribution at $|\mathbf{w}| \approx 1$ in the solar wind frame and cool to small $|\mathbf{w}|$-values.

[61] Here, $g(R)$ is assumed to vary as $R^{-\alpha}$, a simple power law with heliocentric distance because n and β are expected to follow this form, and D, the amount of the distribution visible to the instrument, decreases monotonically with increasing R as the pickup ion distribution cools. With this approximation for $n_{\mathrm{obs,ion}}$, measured data from FIPS can be scaled by R^{α} to normalize measurements to a single radial distance.

[62] The largest errors in the approximation $n(R,\theta) \approx n(R)\Theta(\theta)$ will occur for the range 0.1 AU < R < 0.25 AU in equation (B3), where the downwind enhancement varies by about 50% for the electron-impact ionization case in section 3. However, consider the other contributions to the integral in equation (B3). For all neutral density distributions and ionization profiles from section 3.2, the scaled production rate $R^2\beta n$ increases with radial distance from the Sun inside of 0.25 AU. Furthermore, for both SWICS and FIPS, $D(|\mathbf{w}|)$ increases with increasing $|\mathbf{w}|$. Therefore, any contribution to the integral in equation (B3) in the range 0.1 AU < R < 0.25 AU should have minimal impact on the total instrument-observed densities, even for MESSENGER/FIPS at R = 0.3 AU.

[63] **Acknowledgments.** The MESSENGER project is supported by the NASA Discovery Program under contracts NAS5-97271 to The Johns Hopkins University Applied Physics Laboratory and NASW-00002 to the Carnegie Institution of Washington. This work was also supported by the NASA Graduate Student Research Program grant NNX09AL50H (DJG), and the National Science Foundation grant AGS-1043012 (LAF).

References

Abramenko, V., V. Yurchyshyn, J. A. Linker, Z. Mikić, J. Luhmann, and C. O. Lee (2010), Low-latitude coronal holes at the minimum of the 23rd solar cycle, *Astrophys. J.*, *712*, 813–818.

Andrews, G. B., et al. (2007), The Energetic Particle and Plasma Spectrometer instrument on the MESSENGER spacecraft, *Space Sci. Rev.*, *131*, 523–556.

Auchère, F., D. R. McMullin, J. W. Cook, J. S. Newmark, R. von Steiger, and M. Witte (2005), A model for solar EUV flux helium photoionization throughout the 3-dimensional heliosphere, in *Solar Wind 11/SOHO 16, "Connecting Sun and Heliosphere" Conference,* edited by B. Fleck, T. H. Zurbuchen, and H. Lacoste, Spec. Pub. SP-592, pp. 327–329, European Space Agency, Noordwijk, Netherlands.

Blum, P. W., and H. J. Fahr (1970), Interaction between interstellar hydrogen and the solar wind, *Astron. Astrophys.*, *4*, 280–290.

Blum, P. W., J. Pfleiderer, and C. Wulf-Mathies (1975), Neutral gases of interstellar origin in interplanetary space, *Planet. Space Sci.*, *23*, 93–105.

Bzowski, M., et al. (2012), Neutral interstellar helium parameters based on IBEX-Lo observations and test particle calculations, *Astrophys., J. Suppl. Ser.*, *198,* 12, 1–40.

Drews, C., L. Berger, R. F. Wimmer-Schweingruber, A. B. Galvin, B. Klecker, and E. Möbius (2010), Observations of interstellar neon in the helium focusing cone, *J. Geophys. Res.*, *115*, A10108, doi: 10.1029/2010JA015585.

Fahr, H. J. (1968), On the influence of neutral interstellar matter on the upper atmosphere, *Astrophys. Space Sci.*, *2*, 474–495.

Fahr, H. J. (1971), The interplanetary hydrogen cone and its solar cycle variations, *Astron. Astrophys.*, *14*, 263–274.

Fahr, H. J. (1978), Change of interstellar gas parameters in stellar-wind-dominated astrospheres solar case, *Astron. Astrophys.*, *66*, 103–117.

Feldman, W. C., J. J. Lange, and F. Scherb (1972), Interstellar helium in interplanetary space, in *Solar Wind,* edited by C. P. Sonett, P. J. Coleman Jr., and J. M. Wilcox, Spec. Pub. 308, NASA, Washington, D.C., 684–697.

Fisk, L. A., and L. Zhao (2008), The heliospheric magnetic field and the solar wind during the solar cycle, in *Universal Heliophysical Processes, Symposium S257,* edited by N. Gopalswamy and D. F. Webb, Proceedings of the International Astronomical Union, vol. 4, pp. 109–120, Cambridge Univ. Press, Cambridge, U.K.

Gershman, D. J., T. H. Zurbuchen, L. A. Fisk, J. A. Gilbert, J. M. Raines, B. J. Anderson, C. W. Smith, H. Korth, and S. C. Solomon (2012), Solar wind alpha particles and heavy ions in the inner heliosphere, *J. Geophys. Res.*, *117*, A00M02, doi:10.1029/2012JA017829.

Gilbert, J. A., S. T. Lepri, E. Landi, and T. H. Zurbuchen (2012), First measurements of the complete heavy ion charge state distributions of C, O, and Fe associated with interplanetary coronal mass ejections, *Astrophys. J.*, *751*, 1–8.

Gloeckler, G., and J. Geiss (1998), Interstellar and inner source pickup ions observed with SWICS on Ulysses, *Space Sci. Rev.*, *86*, 127–159.

Gloeckler, G., and J. Geiss (2001), Heliospheric and interstellar phenomena deduced from pickup ion observations, *Space Sci. Rev.*, *97*, 169–181.

Gloeckler, G., N. A. Schwadron, L. A. Fisk, and J. Geiss (1995), Weak pitch angle scattering of few MV rigidity ions from measurements of anisotropies in the distribution function of interstellar pickup H^+, *Geophys. Res. Lett.*, *22*, 2665–2668.

Gloeckler, G., et al. (1998), Investigation of the composition of solar and interstellar matter using solar wind and pickup ion measurements with SWICS and SWIMS on the ACE spacecraft, *Space Sci. Rev.*, *86*, 497–539.

Gloeckler, G., J. Geiss, N. A. Schwadron, L. A. Fisk, T. H. Zurbuchen, F. M. Ipavich, R. von Steiger, H. Balsiger, and B. Wilken (2000), Interception of comet Hyakutake's ion tail at a distance of 500 million kilometres, *Nature*, *404*, 576–578.

Gloeckler, G., et al. (2004), Observations of the helium focusing cone with pickup ions, *Astron. Astrophys.*, *426*, 845–854.

Hartle, R. E., Jr. E. C. Sittler, K. W. Ogilvie, J. D. Scudder, A. J. Lazarus, and S. K. Atreya (1982), Titan's ion exosphere observed from, Voyager 1, *J. Geophys. Res.*, *87*, 1383–1394.

Ipavich, F. M., A. B. Galvin, G. Gloeckler, D. Hovestadt, B. Klecker, and M. Scholer (1986), Comet Giacobini-Zinner: In situ observations of energetic heavy ions, *Science*, *232*, 366–369.

Isenberg, P. A. (1997), A hemispherical model of anisotropic interstellar pickup ions, *J. Geophys. Res.*, *102*, 4719–4724.

Issautier, K., N. Meyer-Vernet, M. Moncuquet, and S. Hoang (1998), Solar wind radial and latitudinal structure: Electron density and core temperature from, Ulysses thermal noise spectroscopy, *J. Geophys. Res.*, *103*, 1969–1979.

Koutroumpa, D., M. R. Collier, K. D. Kuntz, R. Lallement, and S. L. Snowden (2009), Solar wind charge exchange emission from the helium focusing cone: Model to data comparison, *Astrophys. J.*, *697*, 1214–1225.

Lallement, R., J. C. Raymond, J. Bertaux, E. Quémerais, Y. Ko, M. Uzzo, D. McMullin, and D. Rucinski (2004), Solar cycle dependence of the helium focusing cone from SOHO/UVCS observations, Electron impact rates and associated pickup ions, *Astron. Astrophys.*, *426*, 867–874

Maksimovic, M., S. P. Gary, and R. M. Skoug (2000), Solar wind electron suprathermal strength and temperature gradients: Ulysses observations, *J. Geophys. Res.*, *105*, 18,337–18,350.

McComas, D. J., et al. (2004a), The Interstellar Boundary Explorer (IBEX), in *Physics of the Outer Heliosphere Conference,* edited by V. Florinski, G. P. Zank, and N. V. Pogorelov, Conference Proceedings, vol. 719, pp. 162–181, American Institute of Physics, Melville, N.Y.

McComas, D. J., et al. (2004b), The interstellar hydrogen shadow: Observations of interstellar pickup ions beyond Jupiter, *J. Geophys. Res.*, *109*, A02104, doi:10.1029/2003JA010217.

McComas, D. J., R. W. Ebert, H. A. Elliott, B. E. Goldstein, J. T. Gosling, N. A. Schwadron, and R. M. Skoug (2008), Weaker solar wind from the polar coronal holes and the whole Sun, *Geophys. Res. Lett.*, *35*, L18103, doi:10.1029/2008GL034896.

McMullin, D. R., D. L. Judge, E. Phillips, M. Hilchenbach, P. Bochsler, P. Wurz, E. Moebius, and F. Ipavich (2002), Measuring the ionization rate of in-flowing interstellar helium with the SOHO/CELIAS/SEM, in *From, Solar Min to Max: Half a Solar Cycle with SOHO, Proceedings of the SOHO 11 Symposium,* edited by A. Wilson, Spec. Pub. SP-508, pp. 489–491, European Space Agency, Noordwijk, The Netherlands.

McMullin, D. R., et al. (2004), Heliospheric conditions that affect the interstellar gas inside the heliosphere, *Astron. Astrophys.*, *426*, 885–895.

Meier, R. R. (1977), Some optical and kinetic properties of the nearby interstellar gas, *Astron. Astrophys.*, *55*, 211–219.

Möbius, E., D. Hovestadt, B. Klecker, M. Scholer, G. Gloeckler, and F. M. Ipavich (1985), Direct observation of He^+ pick-up ions of interstellar origin in the solar wind, *Nature*, *318*, 426–429.

Möbius, E., D. Rucinski, D. Hovestadt, and B. Klecker (1995), The helium parameters of the very local interstellar medium as derived from the distribution of He^+ pickup ions in the solar wind, *Astron. Astrophys.*, *304*, 505–519.

Möbius, E., et al. (1996), The local interstellar medium viewed through pickup ions, recent results and future perspectives, *Space Sci. Rev.*, *78*, 375–386.

Möbius, E., et al. (2004), Synopsis of the interstellar He parameters from combined neutral gas, pickup ion and UV scattering observations and related consequences, *Astron. Astrophys.*, *426*, 897–907.

Möbius, E., et al. (2010), He pickup ions in the inner heliosphere—Diagnostics of the local interstellar gas and of interplanetary conditions, in *Pickup Ions throughout the Heliosphere and Beyond: Proceedings of the 9th Annual International Astrophysics Conference,* edited by J. LeRoux, G. P. Zank, A. J. Coates, and V. Florinski, Conference Proceedings, vol. 1302, pp. 37–43, American Institute of Physics, Melville, N.Y.

Möbius, E., et al. (2012), Interstellar gas flow parameters derived from Interstellar Boundary Explorer-Lo observations in 2009 and 2010: Analytical analysis, *Astrophys. J. Suppl. Ser.*, *198*, 1–18.

Neugebauer, M., A. J. Lazarus, H. Balsiger, S. A. Fuselier, F. M. Neubauer, and H. Rosenbauer (1989), The velocity distributions of cometary protons picked up by the solar wind, *J. Geophys. Res*, *94*, 5227–5239.

Noda, H., T. Terasawa, Y. Saito, H. Hayakawa, A. Matsuoka, and T. Mukai (2001), Observation of the interstellar helium cone by the NOZOMI spacecraft, *Space Sci. Rev.*, *97*, 423–426.

Raines, J. M., J. A. Slavin, T. H. Zurbuchen, G. Gloeckler, B. J. Anderson, D. N. Baker, H. Korth, S. M. Krimigis, and J. R. L. McNutt (2011), MESSENGER observations of the plasma environment near Mercury, *Planet. Space. Sci.*, *59*, 2004–2015.

Rucinski, D., and H. J. Fahr (1989), The influence of electron impact ionization on the distribution of interstellar helium in the inner heliosphere - possible consequences for determination of interstellar helium parameters, *Astron. Astrophys.*, *224*, 290–298.

Rucinski, D., M. Bzowski, and H. J. Fahr (2003), Imprints from the solar cycle on the helium atom and helium pickup ion distributions, *Annal. Geophys.*, *21*, 1315–1330.

Samson, J. A. R., Z. X. He, L. Yin, and G. N. Haddad (1994), Precision measurements of the absolute photoionization cross sections of He, *J. Phys. B*, *27*, 887–898.

Saul, L., et al. (2003), SOHO CTOF observations of interstellar, He^+ pickup ion enhancements in solar wind compression regions, in *Solar Wind Ten: Proceedings of the Tenth International Solar Wind Conference,* edited by M. Velli, F. Malara, and R. Bruno, Conference Proceedings, vol. 679, pp. 778–781, American Institute of Physics, Melville, N.Y.

Saul, L., E. Möbius, P. A. Isenberg, and P. Bochsler (2007), On pitch-angle scattering rates of interstellar pickup ions as determined by in situ measurement of velocity distributions, *Astrophys. J.*, *655*, 672–677.

Saul, L., P. Wurz, and R. Kallenbach (2009), A measurement of the adiabatic cooling index for interstellar helium pickup ions in the inner heliosphere, *Astrophys. J.*, *703*, 325–329.

Schwadron, N. A. (1998), A model for pickup ion transport in the heliosphere in the limit of uniform hemispheric distributions, *J. Geophys. Res.*, *103*, 20,643–20,650.

Solomon, S. C., et al. (2001), The MESSENGER mission to Mercury: Scientific objectives and implementation, *Planet. Space Sci.*, *49*, 1445–1465.

Stone, E. C., A. M. Frandsen, R. A. Mewaldt, E. R. Christian, D. Margolies, J. F. Ormes, and F. Snow (1998), The Advanced Composition Explorer, *Space Sci. Rev.*, *86*, 1–22.

Thomas, G. E. (1978), The interstellar wind and its influence on the interplanetary environment, *Annu. Rev. Earth Planet. Sci.*, *6*, 173–204.

Vallerga, J., R. Lallement, M. Lemoine, F. Dalaudier, and D. McMullin (2004), EUVE observations of the helium glow: Interstellar and solar parameters, *Astron. Astrophys.*, *426*, 855–865

Vasyliunas, V. M., and G. L. Siscoe (1976), On the flux and the energy spectrum of interstellar ions in the solar system, *J. Geophys. Res.*, *81*, 1247–1252.

von Steiger, R., N. A. Schwadron, L. A. Fisk, J. Geiss, G. Gloeckler, S. Hefti, B. Wilken, R. F. Wimmer-Schweingruber, and T. H. Zurbuchen (2000), Composition of quasi-stationary solar wind flows from Ulysses/Solar wind ion composition spectrometer, *J. Geophys. Res*, *105*, 27,217–27,238.

Weller, C. S., and R. R. Meier (1981), Characteristics of the helium component of the local interstellar medium, *Astrophys. J.*, *246*, 386–393.

Witte, M., M. Banaszkiewicz, H. Rosenbauer, and D. McMullin (2004), Kinetic parameters of interstellar neutral helium: Updated results from the ULYSSES/GAS-instrument, *Adv. Space Res.*, *34*, 61–65.

Woods, T. N. (2010), Irradiance variations during this solar cycle minimum, in *SOHO-23: Understanding a Peculiar Solar Minimum Conference,* edited by S. R. Cranmer, J. T. Hoeksema, and J. L. Kohl, Conference Series, vol. 426, pp. 63–71, Astronomical Society of the Pacific, San Francisco, Calif.

Woods, T. N., P. C. Chamberlin, J. W. Harder, R. A. Hock, M. Snow, F. G. Eparvier, J. Fontenla, W. E. McClintock, and E. C. Richard (2009), Solar Irradiance Reference Spectra (SIRS) for the 2008 Whole Heliosphere Interval (WHI), *Geophys. Res. Lett.*, *36*, L01101, doi: 10.1029/2008GL036373.

Wu, F. M., and D. L. Judge (1979), Temperature and flow velocity of the interplanetary gases along solar radii, *Astrophys. J.*, *231*, 594–605.

Young, D. T., et al. (2004), Cassini plasma spectrometer investigation, *Space Sci. Rev.*, *114*, 1–112.

Zurbuchen, T. H., et al. (2008), MESSENGER observations of the composition of Mercury's ionized exosphere and plasma environment, *Science*, *321*, 90–92.